CrossMark

Core Mass Function of a Single Giant Molecular Cloud Complex with ∼10,000 Cores

Yue Cao[1,2,3] , Keping Qiu[1,2] , Qizhou Zhang[3] , Yuwei Wang[1,2] , and Yuanming Xiao[4]
[1] School of Astronomy and Space Science, Nanjing University, 163 Xianlin Avenue, Nanjing 210023, People's Republic of China; kpqiu@nju.edu.cn
[2] Key Laboratory of Modern Astronomy and Astrophysics (Nanjing University), Ministry of Education, Nanjing 210023, People's Republic of China
[3] Center for Astrophysics | Harvard & Smithsonian, 60 Garden Street, MS 42, Cambridge, MA 02138, USA
[4] Department of Mathematics, Nanjing University, 163 Xianlin Avenue, Nanjing 210023, People's Republic of China

Abstract

Similarity in shape between the initial mass function (IMF) and the core mass functions (CMFs) in star-forming regions prompts the idea that the IMF originates from the CMF through a self-similar core-to-star mass mapping process. To accurately determine the shape of the CMF, we create a sample of 8431 cores with the dust continuum maps of the Cygnus X giant molecular cloud complex, and design a procedure for deriving the CMF considering the mass uncertainty, binning uncertainty, sample incompleteness, and the statistical errors. The resultant CMF coincides well with the IMF for core masses from a few $M_\odot$ to the highest masses of 1300 $M_\odot$ with a power-law of $dN/dM \propto M^{-2.30\pm0.04}$, but does not present an obvious flattened turnover in the low-mass range as the IMF does. More detailed inspection reveals that the slope of the CMF steepens with increasing mass. Given the numerous high-mass star-forming activities of Cygnus X, this is in stark contrast with the existing top-heavy CMFs found in high-mass star-forming clumps. We also find that the similarity between the IMF and the mass function of cloud structures is not unique at core scales, but can be seen for cloud structures of up to several parsec scales. Finally, our SMA observations toward a subset of the cores do not present evidence for the self-similar mapping. The latter two results indicate that the shape of the IMF may not be directly inherited from the CMF.

Unified Astronomy Thesaurus concepts: Stellar mass functions (1612); Dense interstellar clouds (371); Dust continuum emission (412); Molecular gas (1073); Star forming regions (1565)

1. Introduction

Stellar initial mass function (IMF) depicts the mass distribution for a population of newborn stars and appears to be universal at least within the local galaxies (Offner et al. 2014), yet its origin is still not well understood (Kroupa et al. 2013; Offner et al. 2014). Stars assemble their masses from molecular clouds. Observational studies on Galactic star-forming regions found that the mass distribution of cores— dense, elliptical structures on 0.01–0.1 pc scales[5]—has a shape similar to the IMF but is shifted systematically toward higher masses by a factor of ∼3 (Motte et al. 1998; Testi & Sargent 1998; Alves et al. 2007; Könyves et al. 2015). This discovery prompts the intuitive idea that IMF originates from the core mass function (CMF) via a self-similar core-to-star mass mapping process, i.e., the probability that a core forms a star is constant as long as the core-to-star mass ratio is constant (Motte et al. 1998; Alves et al. 2007; Motte et al. 2018). To understand the physics that drives this resemblance and whether (and if so, how) it is related to the origin of the IMF, it is essential to enlarge the sample size and accurately determine the shape of CMF within a single giant molecular cloud complex.

The Cygnus X giant molecular cloud complex (hereafter Cyg X) is one of the nearest (distance from the Sun of ∼1.4 kpc; Rygl et al. 2012), largest (projected dimension of ∼130 pc), and most massive molecular cloud complexes in the Milky Way. It has a total molecular mass of ∼3 × 10⁶ $M_\odot$ (from Cao et al. 2019), and is representative of the active high-mass star-forming regions in the Galaxy by its numerous H II regions

(Wendker et al. 1991), OB associations (Uyanıker et al. 2001), and star-forming filaments and clumps (Hennemann et al. 2012), and is thus an ideal target for constructing a large sample of cloud structures. The identification of cores in Cyg X was conducted on an H_2 column density (N_{H_2}) map illustrated in Figure 1, which was generated by Cao et al. (2019) with the _hirescoldens_ procedure (Men'shchikov et al. 2012) that fits pixel-by-pixel the Herschel continuum images with a graybody thermal dust emission model (Hildebrand 1983). The map provides abundant and detailed information of the spatial distribution of the cold molecular gas in Cyg X with a dynamic range of 1300 in spatial scale (0.14–180 pc) and 1000 in column density (4×10^{20}–4×10^{23} cm^{-2}), which makes it feasible to study the cloud structures within a single-distance giant molecular cloud with a wide range of physical properties and high statistical significance.

2. Analysis

We design a nonparameterized procedure shown in Figure 2 dedicated to derive a "true" probability distribution of source masses and its uncertainties simultaneously from a source sample. The procedure consists of the following steps: (1) extract sources on a column density map to obtain a real source sample; (2) assess the uncertainty of the mass estimation and derive a series of samples with randomized masses from the real sample; (3) generate a series of randomized mass bins and derive the (raw) mass frequency distributions of the randomized samples; (4) derive a series of pseudo-samples, insert and extract them on the column density map to obtain the extracted pseudo-samples; (5) derive a series of completeness levels as a function of mass by spatially matching the pseudo-samples and the extracted pseudo-samples; (6) correct the raw mass frequency distributions for completeness and obtain a

---
[5] The definition of cores can vary and their sizes can span more than one order of magnitude in different studies, so specifications are needed. In this work our core sample has a median size of 0.3 pc.
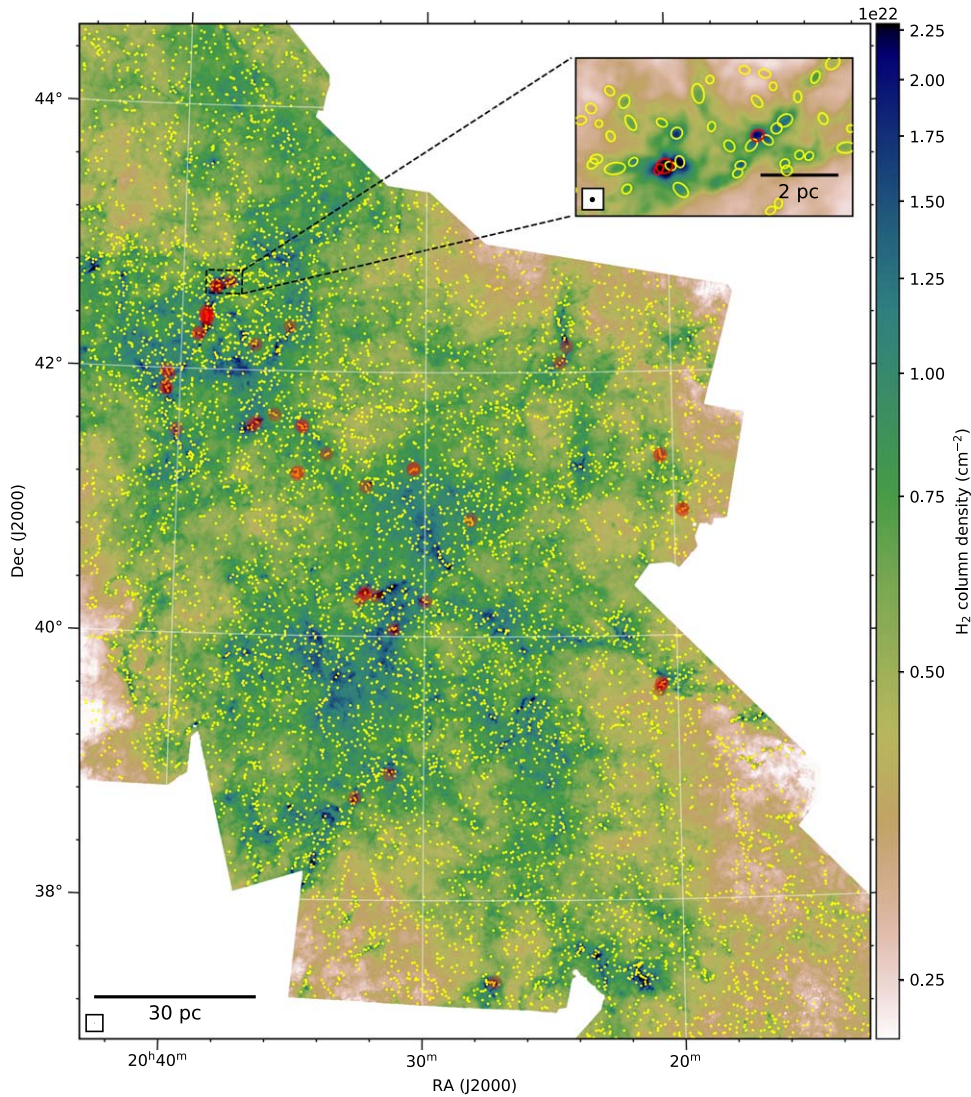
Figure 1. A sample of 8431 cores in Cyg X overlaid on the N_{H_2} map from which they were extracted. In the main panel, positions of all the cores are marked as yellow dots and those as the targets of the SMA high-resolution survey (see Section 3.3) are highlighted in red. The map derived from the Herschel continuum images covers the whole giant molecular cloud with a dynamic range of 1300 in spatial scale and 1000 in column density, making it feasible to generate large samples of cloud structures. The zoom-in panel shows the FWHM ellipses of the cores with the same color coding as in the main panel. Resolution of the map ($20''$) is shown in the lower left corners of both the panels.

series of corrected mass frequency distributions; and (7) reconstruct the true mass probability distribution and its uncertainties based on the statistics of the corrected mass frequency distributions. We argue that this procedure is superior to drawing raw mass distributions (as is done in some literatures) by, first, addressing the sample incompleteness; second, properly estimating all the sources of uncertainties of the mass probability distribution in its derivation process (i.e., mass uncertainty, binning uncertainty, and the uncertainty in completeness levels addressed in steps (2), (3), and (6), respectively); third, greatly reducing the random statistical errors of the mass probability distribution (via a large number of Monte Carlo simulations; see below). Detailed implementations and results of each step are described in Sections 2.1 and 2.2, and more detailed setups, results, and plots of the Monte Carlo simulations in these steps are elaborated in Appendix A. In Section 2.3 we examine the dependence of our results on the source-extraction algorithms. Readers can refer to Section 3.1 for the final results of the derived CMF.

2.1. Source Extraction, Mass Randomization, and Bins Randomization

We used the *getsources* algorithm (Men'shchikov et al. 2012) to extract cores in Cyg X. Designed for identifying dense cloud structures in star-forming regions, *getsources* removes the large-scale background of an image, detects sources by decomposing the image into components on single spatial scales, and measures their properties (coordinates, full width at half maximum (FWHM) diameters, peak column densities, and masses) with the two-dimensional Gaussian model. After a blind run of *getsources* with the N_{H_2} map as input, a total of 12,427 sources were identified. Then we apply the following criteria to select robust detections for deriving the CMF: (1) core mass $M_{core} \geqslant 0.07\ M_{\odot}$; (2) relative core mass uncertainty given by *getsources* $\delta M/M \leqslant 1$; (3) core FWHM diameter no larger than 0.6 pc; (4) cores should be $\geqslant 50''$ away from the map borders to avoid artifacts. Criteria (1) and (3) are dedicated to exclude the implausibly large/small values of the parameters derived by *getsources*. With these criteria 8431 cores with
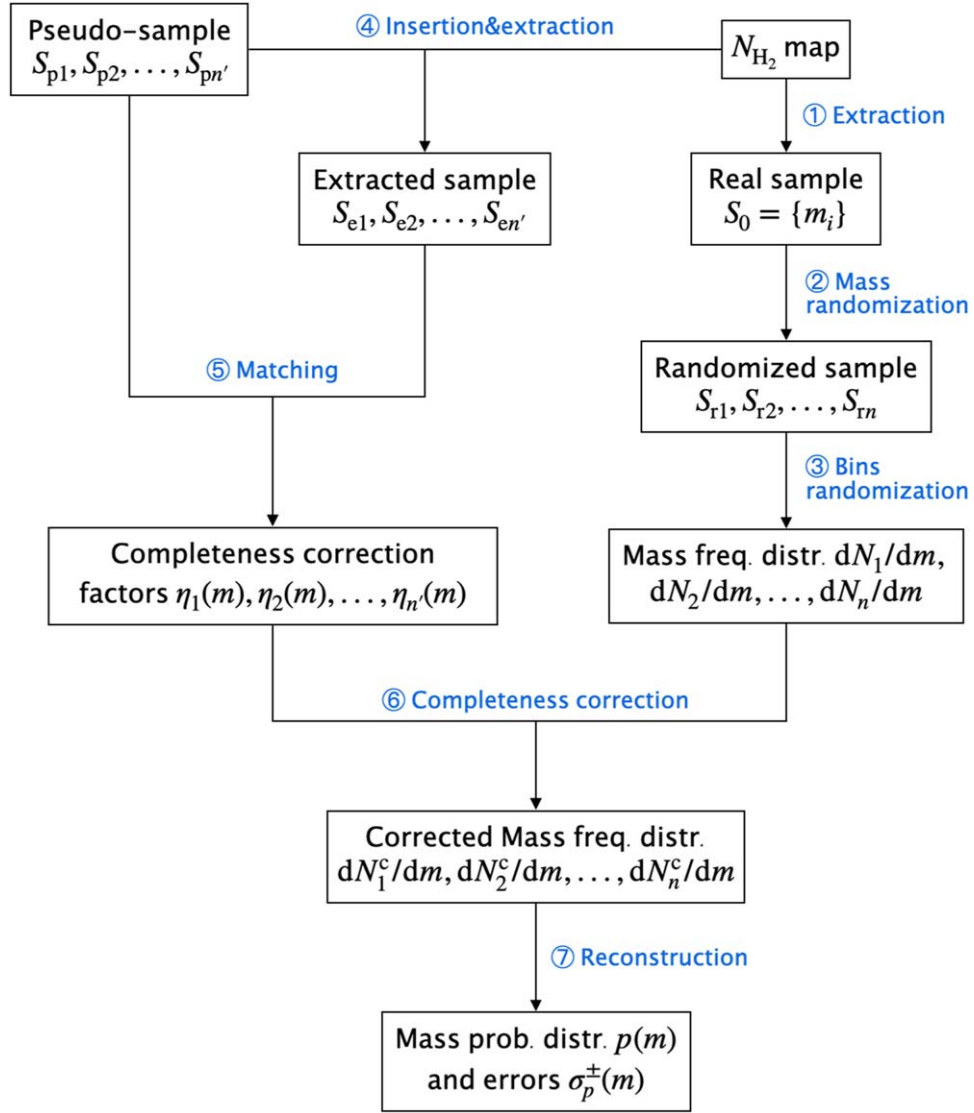
Figure 2. Our designed procedure for deriving a statistically unbiased, "true" mass probability distribution and its uncertainties from a source sample S_0. The text adhered to the arrow lines describes the steps of the procedure and the text in black rectangles represents the intermediate and final results. See Section 2 for detailed descriptions.

robust masses and diameters were selected and their spatial distributions in Cyg X are shown in Figure 1. Statistically, these cores have FWHM diameters ranging from 0.14 to 0.57 pc and masses ranging from 0.1 to 1300 $M_\odot$. Monte Carlo simulations show that the 1σ uncertainty in the core mass evaluation is ~0.23 dex (see Appendix A.1).

To estimate the contribution of the mass uncertainty to the uncertainty of CMF, we generate 100 core samples with the same sample size as the real core sample (8431 cores) and with randomized masses. The mass randomization is implemented by multiplying the real core masses with random factors that simulate the effects of mass uncertainty. The overall effect of this process is that the mass values are randomly shifted by ± 0.23 dex on average. Detailed processes and results of the mass randomization are described in Appendix A.1. We then derive 100 mass frequency distributions with the 100 randomized samples and 100 randomized mass-bin sets. The mass bins are randomized so that the contribution of mass binning to the uncertainty of the mass probability distributions can be addressed. Each randomized bin set has a bin number

close to the square root of the sample size, and a series of random bin centers log-uniformly distributed within the mass range of the sample. For the convenience of further calculations, The 100 mass frequency distributions are then resampled to a fixed set of 90 bins with uniform bin widths in logarithmic mass scales, and to be followed by the completeness correction.

2.2. Completeness Correction and the Derivation of the True Mass Probability Distribution

The completeness level of a sample extracted from a map can never reach 100% due to the noise, background structures on the map, and the performance of the extraction algorithm, and is primarily an increasing function of source mass/flux. Thus the mass/flux distribution of the sample should be corrected by the completeness levels to reflect the true distributions. To derive the completeness level of the core sample of Cyg X as a function of mass, $\eta(M_{core})$, we insert pseudo-cores with a wide range of known masses on the N_{H_2} map and calculate the fractions of the detected ones by *getsources*. This insertion–extraction experiment is done 10
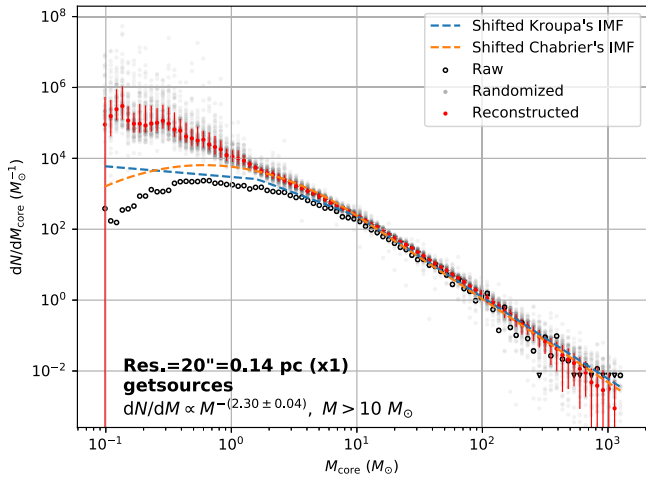
Figure 3. The CMF (true mass probability distribution) of Cyg X derived with the procedure in Figure 2. The solid red line and the associated shaded area illustrate the power-law slope and its error derived in the fitting procedure (see Section 3.1). Blue and orange dashed lines present the shifted IMFs of Kroupa (2001) and Chabrier (2005), respectively, with their starting points of the (most steep) power-law parts pinned at that of the CMF ($10\,M_\odot$). The CMF has been corrected by the completeness levels, and its error bars are derived by considering the effects of mass uncertainty, binning uncertainty, and the uncertainty of completeness levels (see Sections. 2.1 and 2.2).

times to obtain a better estimate of the completeness level and to derive their statistical errors. Detailed setups of the experiments and the derived completeness levels are presented in Appendix A.2. As can be seen, the complete level can be best described as an S-shaped increasing function of mass. The core sample is 90% complete for $M_{\rm core} \geqslant 100\,M_\odot$, and 80% complete for $M_{\rm core} \geqslant 20\,M_\odot$.

We corrected the 100 raw mass frequency distributions in Section 2.1 with the 10 completeness level functions via $dN^{\rm c}/dM_{\rm core} = [dN/dM_{\rm core}]/\eta(M_{\rm core})$. Each completeness level function is used for 10 out of the 100 mass frequency distributions so there is no shortage of completeness levels. The 100 corrected mass frequency distributions are also presented in Appendix A.2.

As a final step, the true probability distribution of the core mass and its 1σ upper/lower error bars are derived as the median values and the lengths of the upper/lower 34 percentile intervals of the 100 corrected mass frequency distributions in individual mass bins, respectively. Figure 3 shows the mass probability distribution and the error bars as the final results. It is clear that the reconstructed distribution is much smoother and steadier than the raw distribution of the core masses, as the former has much fewer statistical errors thanks to the large number (100) of randomized mass distributions in its derivation procedure. To illustrate the individual contributions of the sources of uncertainties (i.e., mass uncertainty, binning uncertainty, and the uncertainty of completeness levels) to the error bars of the mass probability distribution, we go through the processes in Figure 2 again but with only one type of randomization implemented each time, and present the resultant error bars in Appendix A.2. The completeness levels are the most dominant source of uncertainty in the low-mass range, which is reasonable since their values are close to 0 and thus the relative errors are large. In the high-mass range, the uncertainties are dominated by the mass and the binning uncertainties. It is also worth mentioning that a majority of similar studies use the Poisson counting error (proportional to $\sqrt{N}$ for N counts in a bin)

to estimate the binning uncertainty, which can provide similar results to what we present with simulations, but has been proven to be mathematically not rigorous (e.g., the error should not be zero when the count in a bin is zero; see more in Aggarwal & Caldwell 2012).

2.3. Testing the Results with an Alternative Source-extraction Algorithm

So far we have been using *getsources* to extract both real and pseudo-cores in the procedure of deriving the CMF. To examine the dependence of our results on extraction algorithms, we derive the CMF and its uncertainty following the procedure in Figure 2 again but with an alternative algorithm *clumpfind* in the PyCupid[6] (Berry et al. 2007) python package. *Clumpfind* detects sources in an image or a data cube by identifying local peaks and attributing adjacent pixels to the peaks while tracing down the descending contours of the image/cube (Williams et al. 1994). A blind run of *clumpfind* on the $N_{\rm H_2}$ map yields 4974 extracted sources. The reason why the sources are fewer than those identified by *getsources* is that *clumpfind* has poorer detection performance in the low-mass range (see Appendix A.2). We further select 4479 robust cores that are $\geqslant 50''$ away from the map borders to avoid artifacts. These robust cores have masses ranging from 0.49 to 1553 $M_\odot$, and a median FWHM size of 0.29 pc. The resultant mass frequency distributions and the final mass probability distribution, as well as a direct comparison with the results of *getsource*s, are presented in Appendix A.2. As can be seen, the overall shape of the CMF derived with *clumpfind* is very close to that derived with *getsources*, except that the mass range of the *clumpfind* CMF is narrower due to the poorer sensitivity. For $M_{\rm core} \gtrsim 15\,M_\odot$, the *clumpfind* CMF is higher than the *getsources* CMF since *clumpfind* has slightly better detection performance in this mass range. The shapes of the CMFs will be further analyzed in Section 3.1.

3. Discussion

3.1. Shape of the CMF in Cyg X

As is shown in Figure 3, the overall shape of the CMF can be roughly approximated as a single power-law function to the first order. We fit the high-mass part of the CMF with a power-law function to determine its power-law index. The starting point of the CMF for the fitting is determined to be $10\,M_\odot$ using the Ramer–Douglas–Peucker algorithm (Douglas & Peucker 1973), which downsamples a curve into the few most representative points. We use the *curve_fit* function in the SciPy package (Jones et al. 2001) to implement the fitting considering both the values and the uncertainties of the CMF. The fitting yields $dN/dM_{\rm core} \propto M_{\rm core}^{-(2.30\pm0.04)}$ for the high-mass part, and the slope index is close to the canonical values (2.3–2.35) of the IMFs (Salpeter 1955; Kroupa 2001). In Figure 3 we also plot the shifted IMFs of Kroupa (2001) and Chabrier (2005) with their power-law transition points pinned at the starting point of fitting of the CMF. We see that both IMFs are close to the CMF for core masses above a few $M_\odot$. In the low-mass part, the CMF deviates from the IMFs by much larger sample numbers.

With a closer look at the CMF we can find that the slope of the CMF is steepening with increasing mass, which makes the CMF deviate from the single power-law fit (Figure 3). This
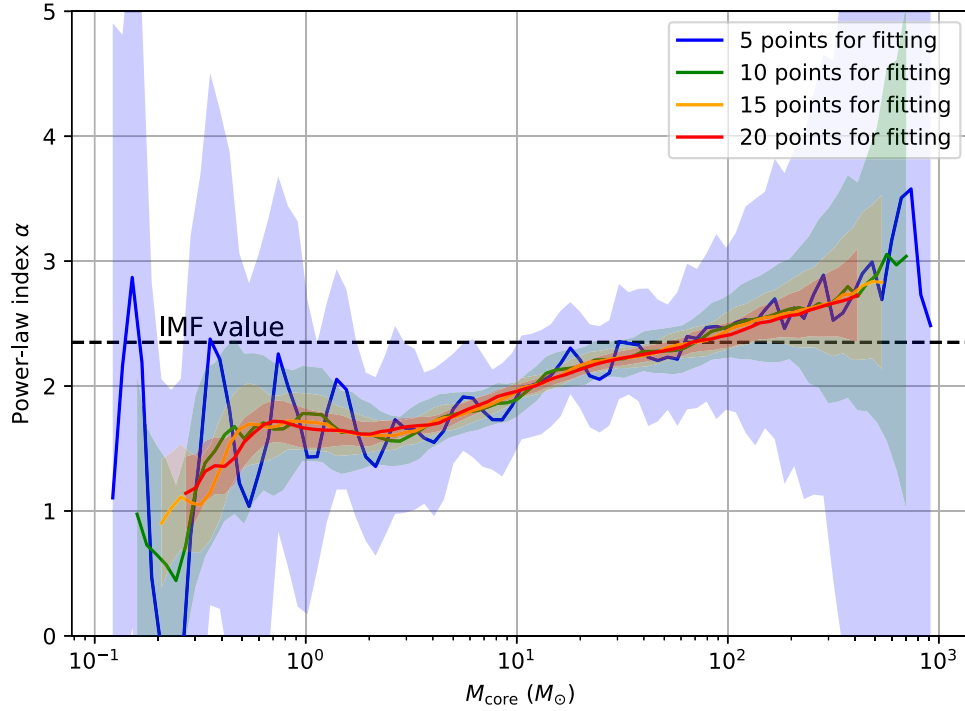
---

6 https://github.com/ChileanVirtualObservatory/pycupid

Figure 4. Power-law index of the CMF in Figure 3 as a function of mass. Lines and shaded areas of different colors illustrate the index values and errors derived with different numbers of consecutive data points used for the fitting. Power-law index of the IMF (2.35) is shown as a horizontal dashed line.

Table 1
Samples of Cloud Structures on Different Spatial Scales

Source sample[a]	gs-20″	gs-40″	gs-60″	gs-80″	gs-160″	gs-320″	cf-20″
Robust source number	8431	2825	1427	821	213	42	4479
Median FWHM diameter (pc)	0.28	0.51	0.72	0.94	1.73	3.29	0.29
Median mass ($M_\odot$)	3.0	14.4	33.1	67.2	322	1262	12.3
Power-law starting point ($M_\odot$)	10	14	28	70	400	1000	38
Power-law index α	2.30 ± 0.04	2.23 ± 0.05	2.10 ± 0.07	2.16 ± 0.11	2.30 ± 0.33	1.89 ± 0.70	2.33 ± 0.05

Note.
[a] "gs" and "cf" for samples derived with *getsources* and *clumpfind*, respectively. The numbers in arcseconds denote the resolutions of the maps from which the sources are extracted.

feature is robustly resolved for CMFs for the first time, thanks to the statistical significance of our core sample and the methods we used to reduce statistical errors. To further illustrate this we plot in Figure 4 the power-law indexes as a function of mass derived with local consecutive data points of the CMF, which again presents a robust increasing trend. Recent observations with submillimeter/millimeter interferometers toward distant ($\geqslant 1$ kpc) high-mass star-forming clumps reveal that the CMFs in these regions have power-law slopes shallower than that of the IMF, presenting a top-heavy feature that is different from the CMFs of nearby low-mass star-forming regions (which resemble the IMF; Motte et al. 2018; Sanhueza et al. 2019; Lu et al. 2020). On the other hand, our finding suggests that on larger scales, the CMF of Cyg X is not top-heavy in the high-mass range, despite the numerous high-mass star-forming regions therein. In fact, most of the cores with $M_{core} \geqslant 200\,M_\odot$ where the CMF shows the cutoff are from the most massive high-mass star-forming regions in Cyg X: DR21, DR21(OH), W75N, DR15, and S106. Several possible scenarios can account for this discrepancy: (1) selection effect of existing interferometric observations since they are focused on high-mass star-forming clumps but not on the entire GMCs;

(2) spacing filtering effect of interferometric observations that makes the lower-mass cores more difficult to detect; and (3) the high-mass star formation in Cyg X is periodic and is now in an inactive phase.

3.2. Mass Functions on Larger Scales

Does such resemblance exist beyond the core scales? Studies using CO low-J rotational transitions found that the mass functions of clouds on at least parsec scales deviate from the shape of the IMF by their shallower power-law tails (Solomon et al. 1987; Williams & McKee 1997; Roman-Duval et al. 2010). However, this may result from the observational biases from the different gas tracers (e.g., CO is less sensitive to high-density regions compared with dust; Hennebelle & Chabrier 2008). To reveal the dependence of mass functions on the spatial scales of cloud structures, we degrade the resolution of the N_{H_2} map (Figure 1) by factors of 2, 3, 4, 8, and 16, respectively, then generate the catalogs of cloud structures on each resolution with *getsources* and derive their mass functions following the same analysis routine as above. Resultant statistical properties of these cloud structures and of their mass functions are summarized in Table 1, and the mass functions of the cloud structures on
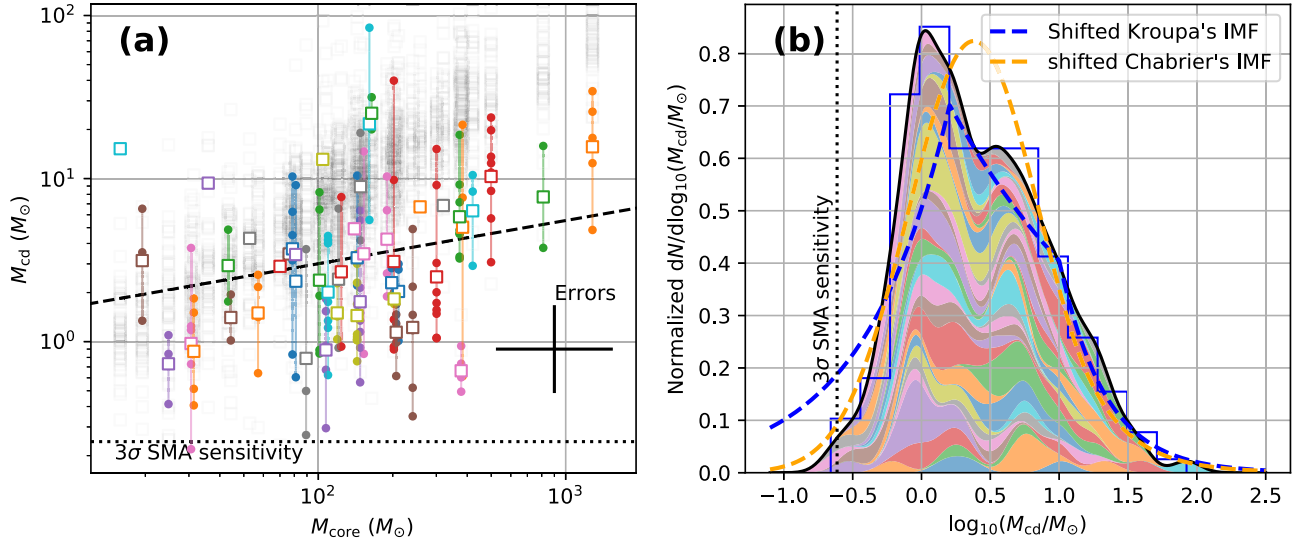
Figure 5. Mass mapping from cores to condensations showing deviations from the predicted mapping scenarios. (a) Relation of core mass versus condensation mass. Each group of monochromatic dots associated with a vertical line represents the condensation masses in each core, with a square denoting their geometric mean value. An isolated square is shown if a core contains only one condensation. Regression analysis of the squares yields $M_{\mathrm{cd, av}} \propto M_{\mathrm{core}}^{0.27 \pm 0.14}$ (black dashed line), which shows a different trend from the pseudo data of the self-similar mapping model generated with Monte Carlo simulations (gray translucent squares). Averaged 3σ detection limit of the SMA maps derived with the noise levels and the parameters in the mass derivation (Appendix A) is shown as dotted lines. Typical error bars in standard deviation values are shown. (b) CdMF (solid black curve and also the blue histogram) of all the 180 condensations and the CdMFs of individual cores as *stacked* colored patches with the same color coding as in panel (a) that contribute to the overall CdMF. CdMFs are generated by a kernel density estimation with a kernel width of 0.2 dex.

different spatial scales are shown in Appendix A.2. It is interesting to see that all the mass functions have similar shapes to the IMF, i.e., presenting a power-law high-mass part and a flattening in the low-mass regime, although the statistical significance drops for the largest spatial scales. This result indicates that the resemblance between the IMF and the mass functions of cloud structures (at least in the high-mass part) is not unique at core scales, but can be extended to at least several parsec scales, which is not consistent with the idea that the shape of the IMF is directly inherited from the CMF.

3.3. Origin of the CMF–IMF Resemblance

How do cores distribute their masses into stars in light of the resemblance among their mass functions? Since it is impossible to trace the whole lifetime of a core observationally, here we focus on the observable core-to-condensation fragmentation to address this problem. Mathematically, there are infinite numbers of ways of core-to-condensation mass mapping even if the two mass functions are identical in shape (see Appendix C for the proofs). Among all the possibilities two intuitive mapping scenarios have been proposed in the literature: (1) self-similar mapping (Motte et al. 1998; Alves et al. 2007; Motte et al. 2018), where the probability that a core of mass M_{core} forms a condensation of mass M_{cd} is constant as long as $M_{\mathrm{core}}/M_{\mathrm{cd}}$ is constant; and (2) internal-IMF mapping (Beuther & Schilke 2004; Shadmehri & Elmegreen 2011), where the underlying condensation mass function (CdMF) in each core is identical to the IMF. To check the validity of these scenarios, we conducted a high-resolution pilot survey toward 48 selected cores with the Submillimeter Array (SMA) in 1.3 mm (see Appendix B), aimed at resolving the cores into condensations with a synthesized beam of $\sim 1{\farcs}8$ (0.012 pc@1.4 kpc), which is more than one order of magnitude smaller than the average core diameter. The target cores were chosen in the high-mass range of the core sample ($>10\ M_{\odot}$) for better detections and to better demonstrate the mass mapping in the more featured and reliable power-law part of the CMF. They were also selected to be absent

from the strong free–free emissions of the ultracompact H II regions in Cyg X (Cao et al. 2019) so that the condensation masses can be properly estimated with the continuum fluxes, which are dominated by thermal dust emissions. Figure 1 presents the spatial distribution of the target cores in Cyg X and their 1.3 mm continuum images are shown in Appendix B. We use *getsources* to identify condensations in the SMA images and selected 200 robust condensations with $\geqslant 5\sigma$ detections (see Appendix B). To generate the core-condensation correspondence, we associated each condensation with the nearest core of which the FWHM ellipse covers the condensation. As a result, 180 condensations are associated with the 48 target cores. The FWHM diameters of these condensations fitted with two-dimensional Gaussians range from 0.008 to 0.05 pc (see 0.14–0.57 pc for the cores). Using the dust temperature map of Cyg X in Cao et al. (2019) and an approximate radiative transfer model (Motte & André 2001; Motte et al. 2018), we estimated the dust temperatures and masses of the condensations (see Appendix B), which range in 14–58 K and 0.2–84 $M_{\odot}$, respectively.

Figure 5 presents the core mass versus condensation mass relation (Figure 5(a)) and the contribution of individual CdMF of each core to the overall CdMF (Figure 5(b)). Regression analysis on the mean condensation mass in each core versus the core mass yields $M_{\mathrm{cd, av}} \propto M_{\mathrm{core}}^{0.27 \pm 0.14}$ with a low correlation coefficient of $R = 0.27$, which is different from the $M_{\mathrm{cd, av}} \propto M_{\mathrm{core}}$ relation predicted by the self-similar mapping model (see Appendix D). To further corroborate this difference, we ran Monte Carlo simulations to generate pseudo condensation masses for each core following the self-similar mapping routine, with the condensation numbers and core-to-condensation formation efficiency mimicking the real data (see also Figure 5). After 500 iterations we derive a mass relation with the pseudo data: $M_{\mathrm{cd, av}} \propto M_{\mathrm{core}}^{1.00 \pm 0.11}$, which indicates that the observed core-to-condensation mass mapping is highly unlikely to be reproduced by the self-similar model. To examine the validity of the internal-IMF model, we performed the two-sided Kolmogorov–Smirnov test with the core/condensation masses as input and with the null hypothesis that the CdMF in

each core has the shape of the IMF regardless of the core mass. The derived p-value is 0.014, which indicates that this model cannot reproduce the observed results. Moreover, in Figure 5(b), the mass distribution of condensations in each core greatly varies from case to case, and is clearly different from the IMF, apparently inconsistent with the internal-IMF model. The cumulative CdMF of all the condensations from all the observed cores has a shape relatively more comparable with the IMF, but there is still deviation in between. The evidence against both scenarios proposed in the literature points to the chaotic nature of the core-to-condensation (and probably also core-to-star) mass mapping process, and implies that any intuitive scenario proposed without full understanding of the underlying physics may oversimplify the reality and fail to explain it.

4. Summary

With an unprecedentedly large sample generated in the Cyg X molecular cloud complex and our dedicated procedure of deriving the CMF and its uncertainty, we accurately reveal the shape of the CMF. We find that the CMF has a power-law tail with a slope index of 2.30 ± 0.04, very close to that of the IMF values, while there is no significant flattening in the low-mass part as presented in IMFs. More detailed analyses illustrate that the slope of the CMF steepens with increasing masses, in contrast with the top-heavy IMFs discovered with recent interferometric observations. This can be explained by the incompleteness of the latter observations, space filtering effect of interferometers, or that the high-mass star formation of Cyg X is in its final stage. We also find that the similarity to the IMF is not unique for cores, but can be extended to parsec-scale structures, indicating that this is a scale-free phenomenon. Our SMA observations further reveal that self-similar mass mapping may not be the case of the IMF origin from CMFs.

Appendix A
Details on Deriving the True Mass Probability Distributions and Their Uncertainties

A.1. Mass Uncertainty and Randomization

Source masses derived by the extraction algorithms (*getsources* or *clumpfind*) can be equivalently derived with a graybody dust continuum model (Hildebrand 1983)

$$M = F_\nu D^2 \Gamma / (\kappa_\nu B_\nu(T)), \qquad (A1)$$

where F_ν is the flux density of the source at frequency ν, $D = 1400$ pc is the distance to the Sun, $\Gamma = 100$ is the gas-to-dust
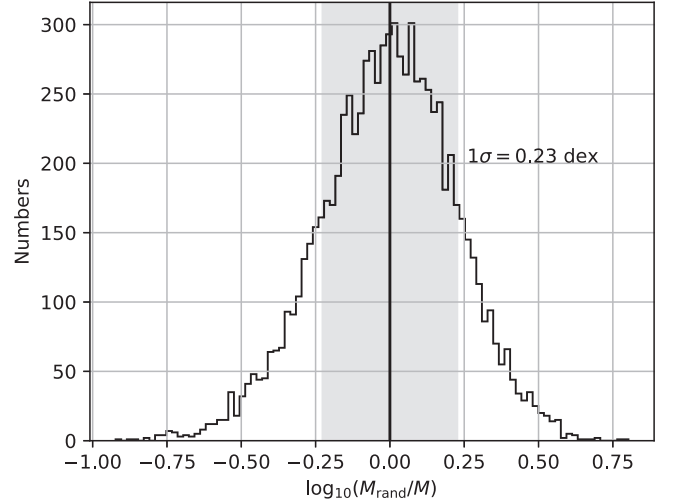

Figure A1. Distribution of the mass randomization factors (i.e., random mass over real mass) with 8000 Monte Carlo realizations (see Appendix A.1). The shaded area shows the standard deviation (0.23 dex) of the distribution.

mass ratio (Hildebrand 1983), $B_\nu(T)$ is the Planck function, T is the dust temperature, and $\kappa_\nu = \kappa_0 (\nu/\nu_0)^\beta$ is the dust mass opacity (Hildebrand 1983), which is evaluated following the HOBYS consortium[7] (e.g., Tigé et al. 2017): $\kappa_0 = 10\,\mathrm{cm}^2\mathrm{g}^{-1}$, $\nu_0 = 1$ THz, and the dust emissivity spectral index $\beta = 2$. The uncertainty in mass mainly comes from the uncertainties in parameters F_ν, D, Γ, T, and β. The 1σ uncertainties of F_ν and T are adopted from Cao et al. (2019) as $\sigma_{F_\nu}/F_\nu = 10\%$ and $\sigma_T = 2$ K, respectively. The uncertainty of D is evaluated as $\sigma_D = 200$ pc based on the parallax measurement results in Rygl et al. (2012). The uncertainties of β and Γ are estimated as $\sigma_\beta = 0.3$ and $\sigma_\Gamma = 20$, respectively. To determine the uncertainty in mass estimates (see Section 2.1), we evaluate these parameters as lognormally distributed random values with the standard deviations mentioned above, and calculate the mass randomization factors (i.e., the ratio between the simulated mass and the real mass) with Equation (A1). Figure A1 illustrates the distribution of the mass randomization factors after $\sim$8000 Monte Carlo realizations, which can be approximated by a lognormal distribution with a standard deviation of $\sim$0.23 dex, i.e., the mass uncertainty of our mass derivation is $\sim$0.23 dex ($\sim$55%).

A.2. Estimating Completeness Levels and Their Uncertainties

For each of the seven source samples presented in Table 1, we perform 10 pseudo-source insertion–extraction experiments to estimate the completeness levels as a function of mass. In each experiment, 3000, 1000, 600, 400, 150, and 60 pseudo-sources modeled as 2D Gaussian functions are randomly positioned on the corresponding original/smoothed N_{H_2} maps on the $\times 1$, $\times 2$, $\times 3$, $\times 4$, $\times 8$, and $\times 16$ scales, respectively. The pseudo-sources have log-uniformly distributed masses covering the mass range of the real sources, and sizes following the distributions of the real source sizes. *Getsources* and *clumpfind* are used to extract the pseudo-sources on the $\times$1–16 maps and the $\times$1 map, respectively. Similar criteria as described in Section 2.1 are used to select robust sources in each experiment. See Table A1 for the detailed

Table A1
Generation and Extraction of the Samples of Pseudo-sources

Sample[a]	Pseudo-source No.[b]	Min Mass[c] ($M_\odot$)	Border Width[d] ($''$)	Extracted Source No.[e]	Max Separation[f] (pc)	Matched Source No.[g]	Matching Rate[h]
gs-20$''$-1	3000	0.001	22	12570	0.025	1711	57.0%
gs-20$''$-2	3000	0.001	22	11981	0.025	1659	55.3%
gs-20$''$-3	3000	0.001	22	12060	0.025	1645	54.8%
gs-20$''$-4	3000	0.001	22	12042	0.025	1602	53.4%
gs-20$''$-5	3000	0.001	22	12180	0.025	1623	54.1%
gs-20$''$-6	3000	0.001	22	12258	0.025	1652	55.1%
gs-20$''$-7	3000	0.001	22	12032	0.025	1660	55.3%
gs-20$''$-8	3000	0.001	22	12084	0.025	1648	54.9%
gs-20$''$-9	3000	0.001	22	12116	0.025	1660	55.3%
gs-20$''$-10	3000	0.001	22	11769	0.025	1598	53.3%
gs-40$''$-1	1000	0.001	44	4218	0.05	531	53.1%
gs-40$''$-2	1000	0.001	44	4032	0.05	546	54.6%
gs-40$''$-3	1000	0.001	44	3973	0.05	534	53.4%
gs-40$''$-4	1000	0.001	44	4081	0.05	556	55.6%
gs-40$''$-5	1000	0.001	44	4076	0.05	544	54.4%
gs-40$''$-6	1000	0.001	44	4020	0.05	551	55.1%
gs-40$''$-7	1000	0.001	44	4059	0.05	538	53.8%
gs-40$''$-8	1000	0.001	44	4125	0.05	537	53.7%
gs-40$''$-9	1000	0.001	44	4088	0.05	525	52.5%
gs-40$''$-10	1000	0.001	44	4026	0.05	540	54.0%
gs-60$''$-1	600	0.01	66	2243	0.1	331	55.2%
gs-60$''$-2	600	0.01	66	2219	0.1	320	53.3%
gs-60$''$-3	600	0.01	66	2262	0.1	335	55.8%
gs-60$''$-4	600	0.01	66	2188	0.1	344	57.3%
gs-60$''$-5	600	0.01	66	2220	0.1	332	55.3%
gs-60$''$-6	600	0.01	66	2254	0.1	331	55.2%
gs-60$''$-7	600	0.01	66	2241	0.1	325	54.2%
gs-60$''$-8	600	0.01	66	2283	0.1	348	58.0%
gs-60$''$-9	600	0.01	66	2242	0.1	340	56.7%
gs-60$''$-10	600	0.01	66	2186	0.1	323	53.8%
gs-80$''$-1	400	0.01	88	1475	0.2	241	60.2%
gs-80$''$-2	400	0.01	88	1462	0.2	221	55.2%
gs-80$''$-3	400	0.01	88	1492	0.2	222	55.5%
gs-80$''$-4	400	0.01	88	1482	0.2	221	55.2%
gs-80$''$-5	400	0.01	88	1469	0.2	248	62.0%
gs-80$''$-6	400	0.01	88	1450	0.2	233	58.2%
gs-80$''$-7	400	0.01	88	1501	0.2	224	56.0%
gs-80$''$-8	400	0.01	88	1445	0.2	232	58.0%
gs-80$''$-9	400	0.01	88	1454	0.2	238	59.5%
gs-80$''$-10	400	0.01	88	1453	0.2	218	54.5%
gs-160$''$-1	150	0.1	177	475	0.4	81	54.0%
gs-160$''$-2	150	0.1	177	485	0.4	79	52.7%
gs-160$''$-3	150	0.1	177	484	0.4	76	50.7%
gs-160$''$-4	150	0.1	177	480	0.4	81	54.0%
gs-160$''$-5	150	0.1	177	501	0.4	88	58.7%
gs-160$''$-6	150	0.1	177	499	0.4	81	54.0%
gs-160$''$-7	150	0.1	177	473	0.4	72	48.0%
gs-160$''$-8	150	0.1	177	487	0.4	76	50.7%
gs-160$''$-9	150	0.1	177	491	0.4	83	55.3%
gs-160$''$-10	150	0.1	177	497	0.4	90	60.0%
gs-320$''$-1	60	10	354	154	0.8	28	46.7%
gs-320$''$-2	60	10	354	169	0.8	32	53.3%
gs-320$''$-3	60	10	354	167	0.8	28	46.7%
gs-320$''$-4	60	10	354	152	0.8	28	46.7%
gs-320$''$-5	60	10	354	156	0.8	27	45.0%
gs-320$''$-6	60	10	354	157	0.8	29	48.3%
gs-320$''$-7	60	10	354	164	0.8	30	50.0%
gs-320$''$-8	60	10	354	157	0.8	24	40.0%
gs-320$''$-9	60	10	354	170	0.8	29	48.3%

Table A1
(Continued)

Sample[a]	Pseudo-source No.[b]	Min Mass[c] ($M_\odot$)	Border Width[d] (″)	Extracted Source No.[e]	Max Separation[f] (pc)	Matched Source No.[g]	Matching Rate[h]
gs-320″-10	60	10	354	168	0.8	25	41.7%
cf-20″-1	3000	0.001	22	5757	0.025	1723	57.4%
cf-20″-2	3000	0.001	22	5695	0.025	1647	54.9%
cf-20″-3	3000	0.001	22	5696	0.025	1628	54.3%
cf-20″-4	3000	0.001	22	5654	0.025	1617	53.9%
cf-20″-5	3000	0.001	22	5656	0.025	1626	54.2%
cf-20″-6	3000	0.001	22	5644	0.025	1631	54.4%
cf-20″-7	3000	0.001	22	5719	0.025	1663	55.4%
cf-20″-8	3000	0.001	22	5677	0.025	1652	55.1%
cf-20″-9	3000	0.001	22	5690	0.025	1687	56.2%
cf-20″-10	3000	0.001	22	5617	0.025	1593	53.1%

Notes.
[a] "gs" and "cf" for samples derived with *getsources* and *clumpfind*, respectively. The first number in arcseconds denotes the resolution of the map from which the sources are extracted. The second number is the number of the source insertion–extraction experiment.
[b] Number of pseudo-sources inserted in one experiment.
[c] Minimum mass used to exclude sources with implausibly small extracted mass values.
[d] Sources with distances from the map borders smaller than these values are excluded to avoid artifacts.
[e] Number of extracted robust sources (including both pseudo-sources and real sources) from a map in an experiment.
[f] Maximum separation in parsecs (assuming a distance of 1.4 kpc) used to match the extracted sources and the pseudo-sources.
[g] Number of matched pseudo-sources.
[h] Equals to matched source No./pseudo-source No., which is an estimation of the detection rate of the pseudo-sources.
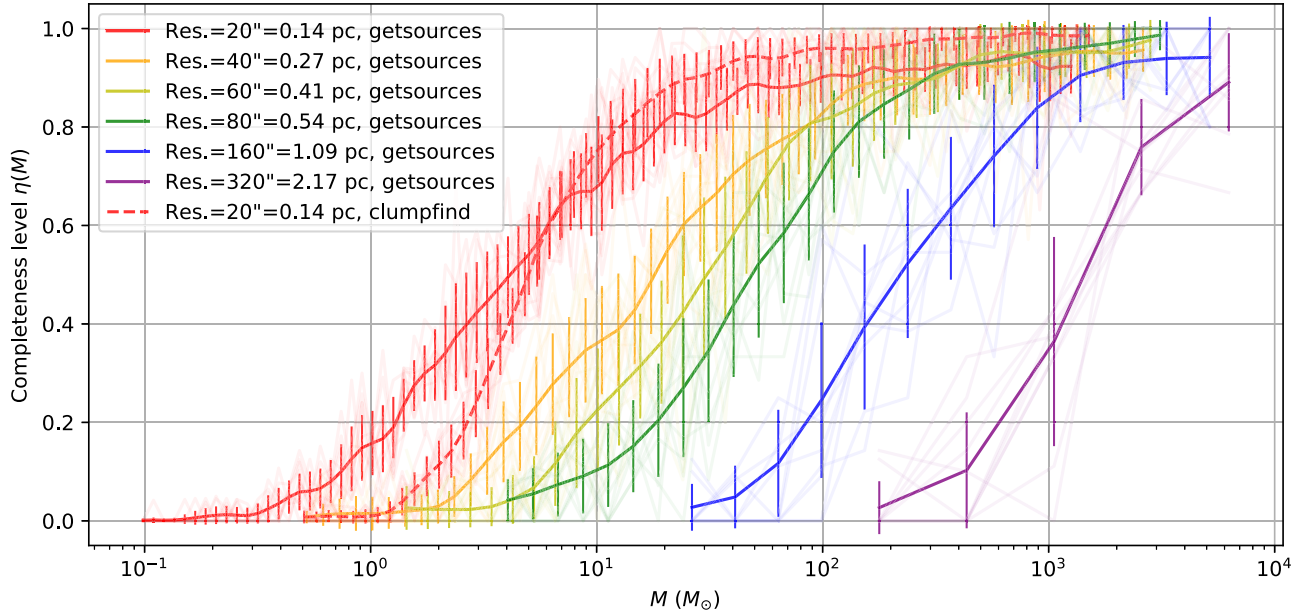

Figure A2. Completeness levels of the samples of cloud structures as a function of mass, derived via pseudo-source insertion–extraction experiments (see Section 2.2 and Appendix A.2). The pale-colored curves are completeness levels derived in individual experiments and the bright-colored ones are the means of the former. Error bars of the completeness levels are estimated as the standard derivations of the pale-colored curves. Only the pale-colored curves are used in the completeness correction process to include the contribution of the uncertainties of the completeness levels to the uncertainties of the derived mass probability distributions (see Section 2.2).

information of the source samples in all the experiments. Finally, Figure A3 shows mass distributions of six source samples obtained with *getsources* on the smoothed column density maps and one sample derived with *clumpfind* on the original column density map. Figure A4 visualizes the contributions from the mass uncertainty, binning uncertainty, and the completeness level uncertainty to the error bars of the reconstructed mass probability

distribution. Figure A5 presents a direct comparison between the mass probability distributions obtained with the *getsources* and *clumpfind* algorithms.

The extracted sources in an experiment contain both real and pseudo-sources. We spatially match the inserted pseudo-sources and the extracted sources with maximum allowed separations listed in Table A1, with which the two matched
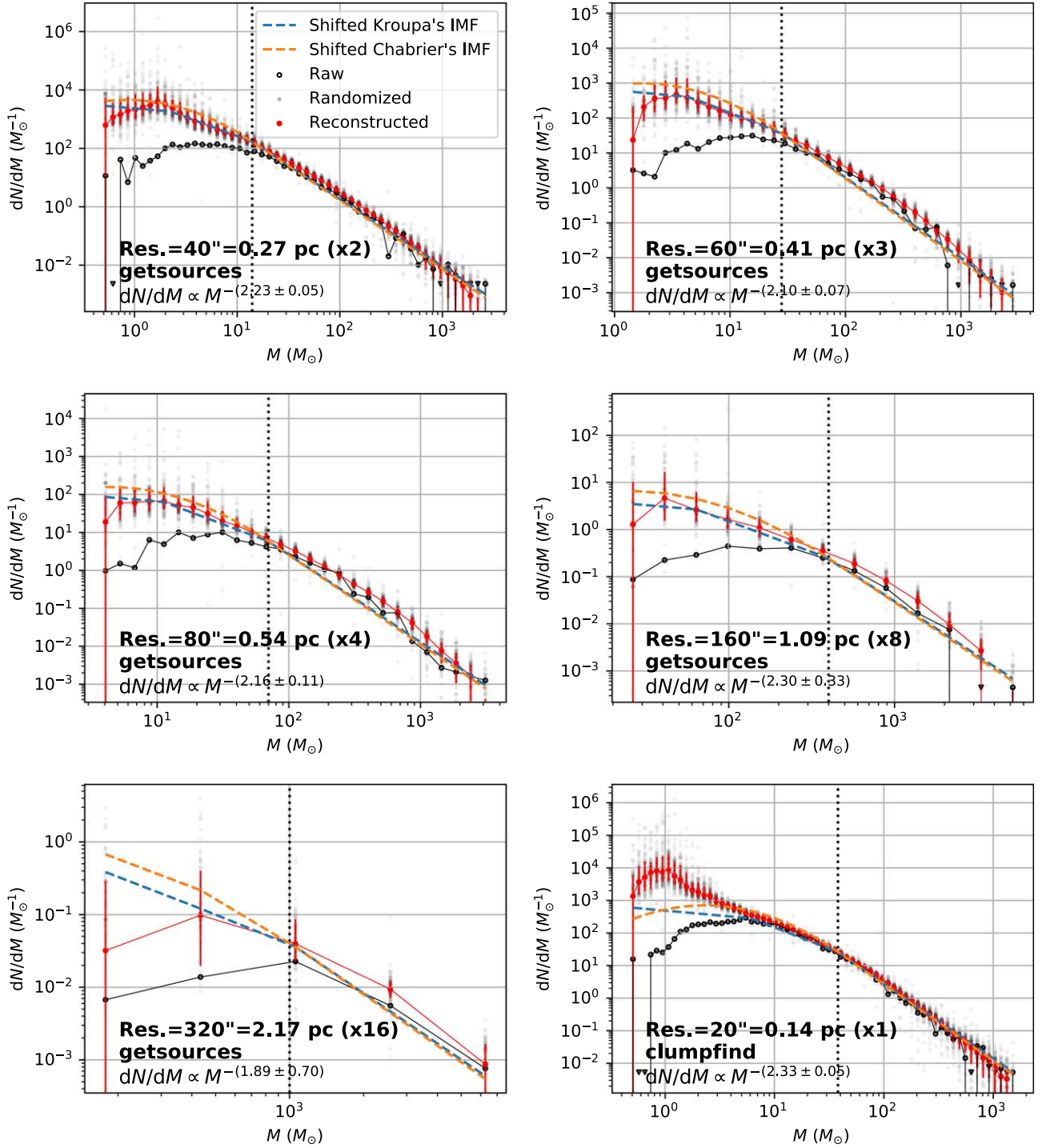
Figure A3. Mass distributions of the samples of cloud structures. Raw distributions (black circles/triangles) are drawn using the source masses of the samples, with triangular symbols denoting zero values. Black transparent dots show the 100 randomized, completeness-corrected distributions of each sample (see Section 2). Red dots and error bars present the reconstructed mass probability distributions and their uncertainties derived as the means and the standard deviations of the randomized distributions, respectively (see Section 2.2). Vertical dashed lines show the starting points of the power-law fitting of the high-mass parts and the fitting results are shown in each panel (see Section 3.1). Note that the mass probability distributions (red dots) are not normalized for better comparison.

sources can be considered as one based on eye inspection. The completeness level as a function of mass can then be calculated as the number fraction of the detected pseudo-sources with

masses in a mass bin over the inserted pseudo-sources in that mass bin. Figure A2 presents the completeness levels derived in all the experiments.
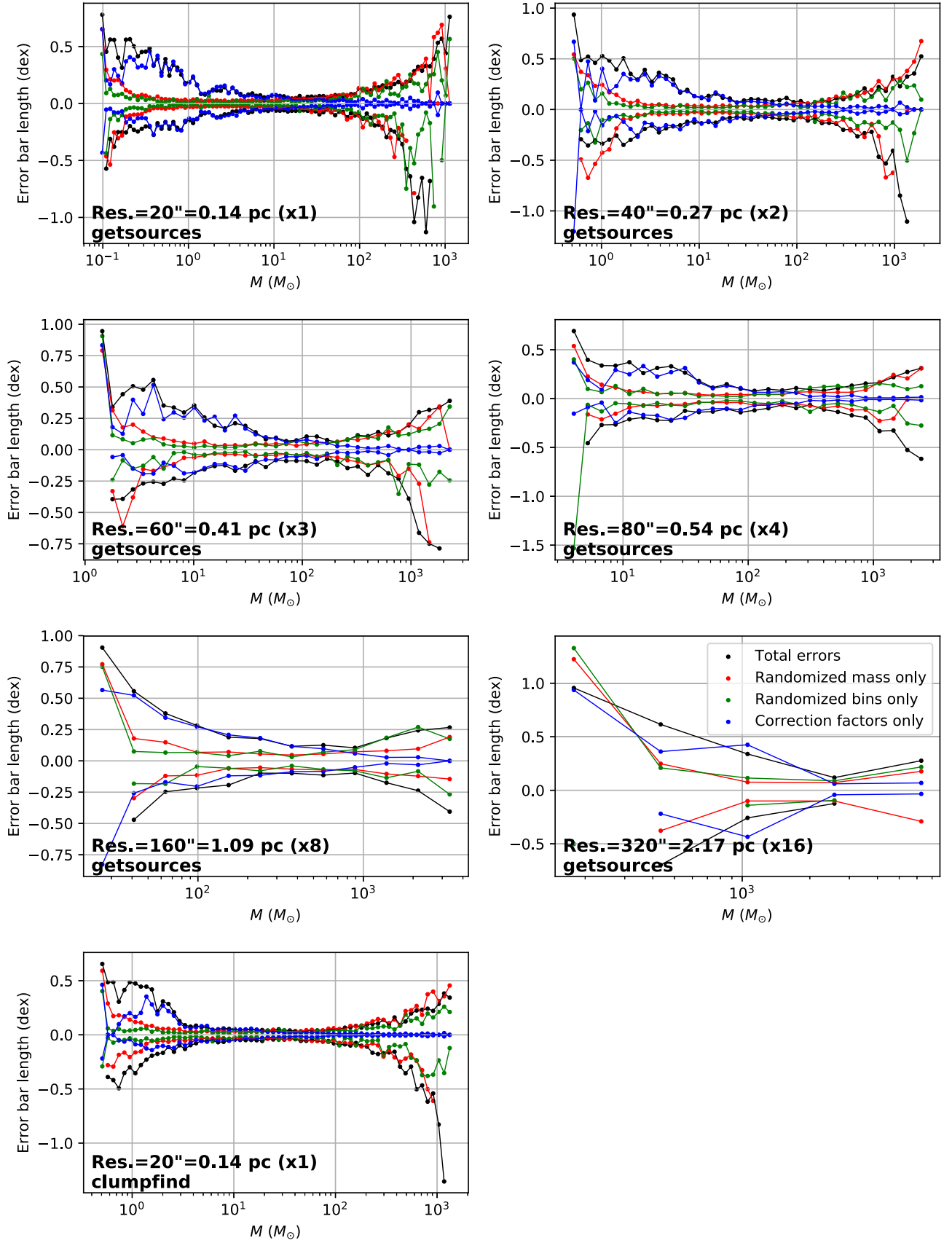
Figure A4. Error bar lengths of the mass probability distributions in Figure D3 as a function of mass. Black, red, green, and blue curves represent the total errors, errors from mass uncertainties, errors from binning uncertainties, and errors from completeness levels, respectively (see Section 2.2). Note that the total errors are not derived from the other errors directly so they can happen to be smaller than the other ones in some plots.
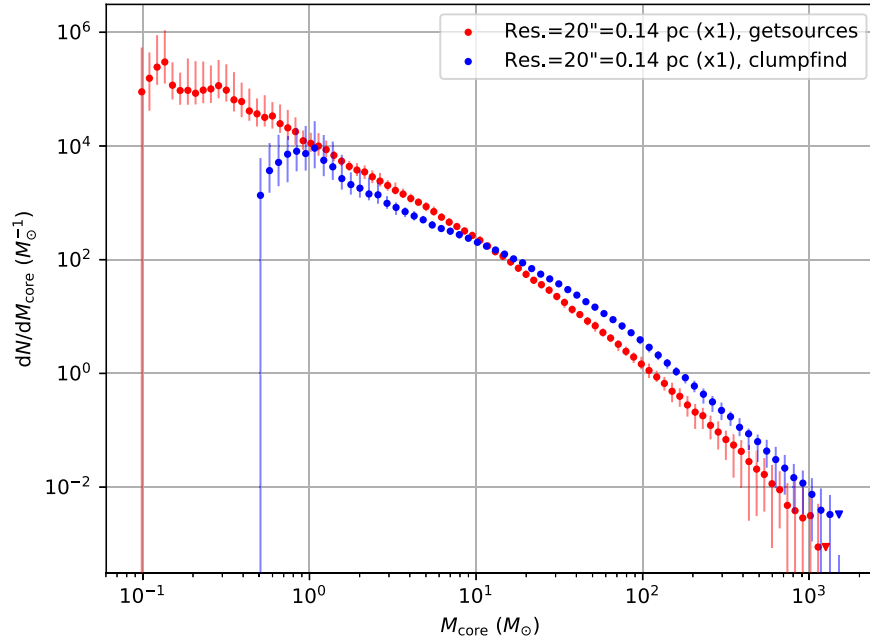
Figure A5. Mass probability distributions of the cores derived with *getsources* and *clumpfind*, respectively, for comparison (see Section 2.3).

Appendix B
High-resolution Pilot Survey Resolving the Cores into Condensations

High-resolution observations toward 48 cores in the high-mass range ($M_{\rm core} \geqslant 10\ M_{\odot}$) of the core sample were conducted with the SMA at the 1.3 mm continuum band in the "compact" and "extended" array configurations during years 2015–2016 (project code: 2015A-S068, 2015A-S072, and 2016A-S061; PI: Keping Qiu). The target cores are absent from the strong free–free emissions from the ionized components of the ultracompact H II regions in Cyg X (Cao et al. 2019), allowing us to better constrain the masses of the condensations with the 1.3 mm emissions. We used the Miriad (Sault et al. 1995) software to conduct the data reduction and combine the data in the two configurations to make images. The final products contain 31 single-field images and two mosaic images (see Figure B1). These images recover the continuum emissions on spatial scales from their synthesized beams of ∼1″8 (0.012 pc@1.4 kpc) to the largest angular scale of ∼20″ (0.14 pc), the latter of which is very close to the resolution of the $N_{\rm H_2}$ map. The 1σ rms noise level of these images is ∼1.0 mJy·beam^{-1} on average, evaluated over the emission-free regions.

A blind extraction of *getsources* on the 33 images yielded 923 detections, among which a large proportion are false detections caused by image noises and the artifacts on the image borders. With a criterion that source flux (before the primary-beam correction) must be above the 5σ values of the image noise levels, the bad detections can be easily removed and the sample is reduced to 200 robust condensations. Primary-beam correction was then applied to the fluxes and peak intensities of these condensations to eliminate the effect of the antenna angular response. These condensations have FWHM diameters ranging from 0.008–0.05 pc, and 1.3 mm continuum fluxes ranging from 0.006–1.2 Jy.

Dust temperatures of the condensations were estimated by combining the two results of (1) the large-scale (resolution∼36″) dust temperature map of Cyg X in (Cao et al. 2019; see their Figure 26), and (2) an approximate radiative transfer model

(Motte & André 2001) for calculating the temperature distribution on small ($\leqslant 0.1$ pc) scales, following the idea of Motte et al. (2018). The former was produced together with the $N_{\rm H_2}$ map by fitting pixel-by-pixel the Herschel continuum images of Cyg X, and the latter formulates a power-law radial temperature profile $T(r) \propto r^{-0.4} L_{\star}^{0.2}$ (see Equation (2) of Motte & André 2001), where $L_{\star}$ is the luminosity of the central heating source (protostars). This decreasing temperature profile with radius will reach the large-scale temperature level at some radius $r_{\rm isoth}$ (see Equation (3) of Motte & André 2001), out of which the temperature has negligible difference with the values in the large-scale temperature map. The actual temperature profile of a condensation is thus a piecewise function containing a power-law part for $r \leqslant r_{\rm isoth}$ and a flat part for $r > r_{\rm isoth}$. If a condensation does not have associated protostars, $r_{\rm isoth} = 0$ and the temperature profile contains only the flat part. The mean dust temperature of a condensation is estimated by averaging the temperature profile over the condensation volume.

To determine $L_{\star}$ of the central protostars of the condensations, we spatially matched the condensation sample with the AllWISE Source Catalog (Cutri et al. 2014) and the Spitzer Cygnus X Archive Catalog (Kraemer et al. 2010). The AllWISE catalog was used first due to its better spatial coverage and fewer photometrically saturated sources, and the Spitzer catalog was used as supplementary data in case of missing infrared sources. With a maximum allowed separation of 0.01 pc, 51 out of 200 condensations are associated with the AllWISE/Spitzer infrared sources. We integrated the fluxes over all the WISE/Spitzer bands for the 51 condensations to estimate their $L_{\star}$, which ranges from 0.01 to 1160 $L_{\odot}$. As a result, the derived temperatures of the 200 condensations range from 14 to 58 K, with a median value of 21 K.

With the condensation temperature determined, condensation mass can be derived with the same dust emission model as in the derivation of the core mass: $M_{\rm cd} = F_{\nu} D^2 \Gamma / (\kappa_{\nu} B_{\nu}(T))$, where $\nu = 230$ GHz. The other parameters in this equation took the same evaluation as in the derivation of core masses. The resultant masses of the 200 condensations range from 0.2 to 84 $M_{\odot}$, with a
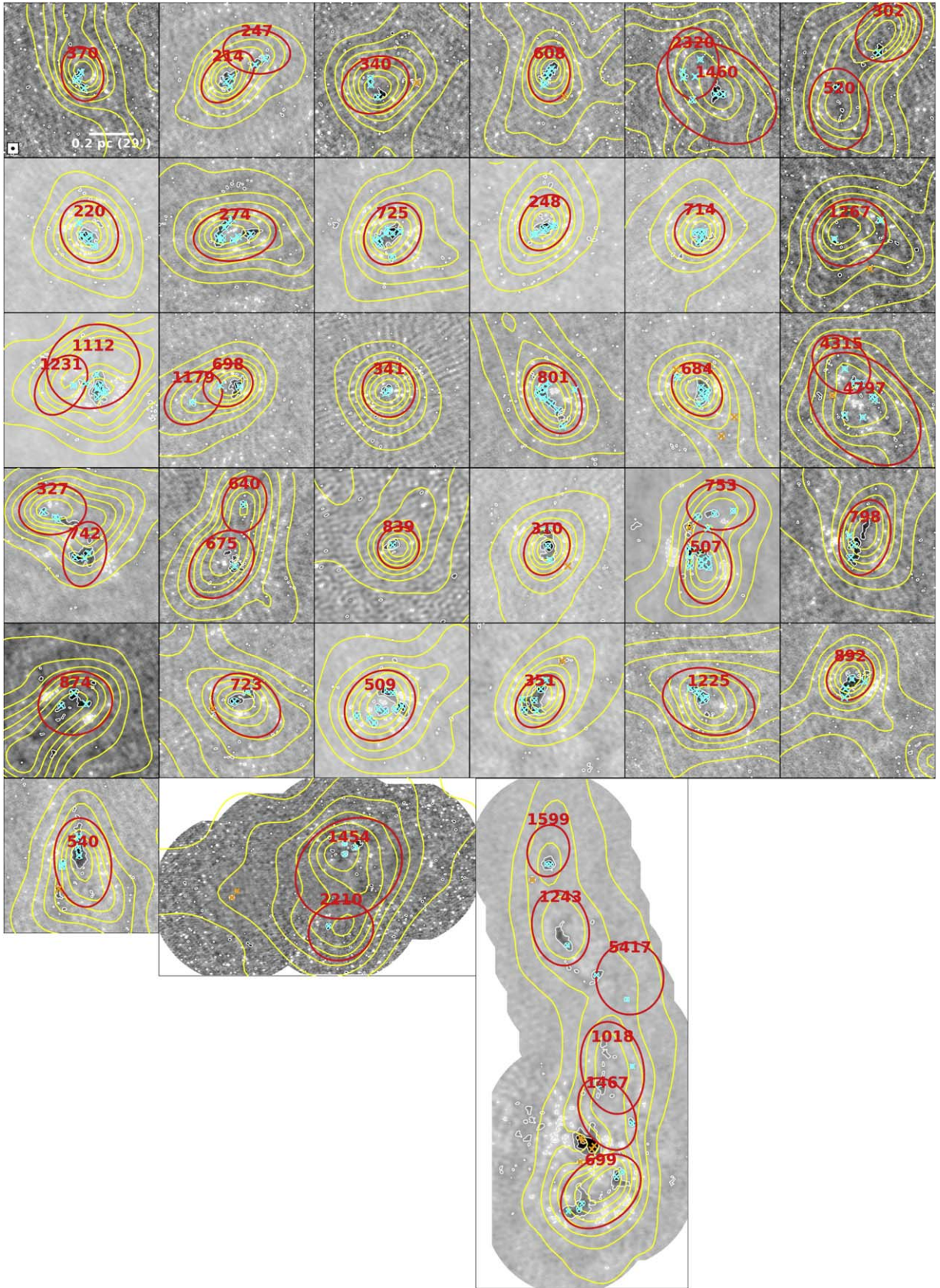
Figure B1. High-resolution 1.3 mm continuum images of SMA observations showing the substructures of the 48 target cores. Grayscales are the 1.3 mm continuum emissions, with higher intensities rendered darker. North is up and east is left. Red ellipses show the FWHM diameters of the cores. Cyan/orange crosses mark the condensations associated/not associated with the cores. Yellow contours of the H_2 column density derived from the Herschel data are drawn linearly from the minimum to the maximum values in the panels. White contours of the 1.3 mm emissions are drawn in $[..., -4^2, -4^1, -4^0, 4^0, 4^1, 4^2,...] \times 3\sigma$, with negative contours shown in white dashed curves. All the panels share the same scale bar and the angular resolution illustrated in the most top-left panel.

median value of 2.2 $M_\odot$. Similar to the method of determining the core mass uncertainty, we conducted Monte Carlo simulations with the following evaluation of the parameter errors: SMA flux uncertainty $\sigma_{F_\nu}/F_\nu = 10\%$, $\sigma_D = 200$ pc, $\sigma_\beta = 0.3$, $\sigma_T = 4$ K, and $\sigma_\Gamma = 20$, and the condensation mass uncertainty is estimated to be ~0.26 dex after 500 simulation runs.

Appendix C
Infinite Possible Ways of Self-similar Mass Mapping

Here we illustrate that there are infinite possible ways of core-to-condensation mass mapping given that CdMF is identical to CMF. Let $F(m_{cl})$ and $G(m_c)$ be the normalized CMF and CdMF, respectively, and $p(m_{cl}, m_c)dm_c$ be the probability that a core of mass m_{cl} forms condensations in the mass interval $[m_c, m_c + dm_c]$. We have $\int F(m_{cl})dm_{cl} = \int G(m_c)dm_c = \int p(m_{cl}, m_c)dm_c = 1$ due to normalization. By definition $G(m_c)$ can be written as

$$G(m_c) = \int F(m_{cl})p(m_{cl}, m_c)dm_{cl}. \tag{C1}$$

Assuming that CdMF is identical to CMF, i.e., $F = G$, and that $p(m_{cl}, m_c)$ can be written as

$$p(m_{cl}, m_c) = G(m_c)f(m_{cl}), \tag{C2}$$

then Equation (C1) becomes

$$1 = \int F(m_{cl})f(m_{cl})dm_{cl}. \tag{C3}$$

Since $F(m_{cl})$ is normalized, there are infinite possible ways of choosing $f(m_{cl})$ to satisfy the above equation (see there are infinite possible ways of choosing a_i to satisfy $\sum a_i x_i = 1$ given $\sum x_i = 1$). In other words, there are infinite ways of mass mapping even if the two mass functions are identical.

Appendix D
Properties of the Self-similar Mass Mapping

Here we illustrate that for self-similar core-to-condensation mass mapping, the mean condensation mass of a core is proportional to the core mass. Self-similarity requires that the probability that a core of mass m_{cl} forms condensations of mass m_c is equal to the one that a core of mass tm_{cl} forms condensations of mass tm_c, i.e.,

$$p(m_{cl}, m_c)dm_c = p(tm_{cl}, tm_c)dtm_c, \tag{D1}$$

where $p(m_{cl}, m_c)$ the probability density, and t is the mass scaling factor. That is,

$$p(m_{cl}, m_c) = t\, p(tm_{cl}, tm_c). \tag{D2}$$

By definition, $p(m_{cl}, m_c)$ is normalized for all m_{cl}, i.e., $\int p(m_{cl}, m_c)dm_c = 1$. For the core of mass m_{cl}, the mean mass of condensations that it produces is

$$\overline{m}_c = \int m_c p(m_{cl}, m_c)dm_c. \tag{D3}$$

For the core of mass tm_{cl} the mean condensation mass is

$$\overline{m}_c = \int tm_c p(tm_{cl}, tm_c)dtm_c = \int tm_c \frac{p(m_{cl}, m_c)}{t}dtm_c$$
$$= t\int m_c p(m_{cl}, m_c)dm_c = t\overline{m}_c, \tag{D4}$$

which means that $\overline{m}_c$ scales as m_{cl} with the same factor t, i.e., $\overline{m}_c$ is proportional to m_{cl}.

ORCID iDs

Yue Cao ⬤ https://orcid.org/0000-0002-6368-7570
Keping Qiu ⬤ https://orcid.org/0000-0002-5093-5088
Qizhou Zhang ⬤ https://orcid.org/0000-0003-2384-6589
Yuwei Wang ⬤ https://orcid.org/0000-0001-6630-0944
Yuanming Xiao ⬤ https://orcid.org/0000-0002-3558-4523

References

Aggarwal, R., & Caldwell, A. 2012, EPJP, 127, 24
Alves, J., Lombardi, M., & Lada, C. J. 2007, A&A, 462, L17
Astropy Collaboration, Robitaille, T. P., Tollerud, E. J., et al. 2013, A&A, 558, A33
Berry, D. S., Reinhold, K., Jenness, T., & Economou, F. 2007, in ASP Conf. Ser. 376, Astronomical Data Analysis Software and Systems XVI, ed. R. A. Shaw, F. Hill, & D. J. Bell (San Francisco, CA: ASP), 425
Beuther, H., & Schilke, P. 2004, Sci, 303, 1167
Cao, Y., Qiu, K., Zhang, Q., et al. 2019, ApJS, 241, 1
Chabrier, G. 2005, in The Initial Mass Function: From Salpeter 1955 to 2005, Astrophysics and Space Science Library, Vol. 327, ed. E. Corbelli, F. Palla, & H. Zinnecker (Dordrecht: Springer), 41
Currie, M. J., Berry, D. S., Jenness, T., et al. 2014, in ASP Conf. Ser. 485, Astronomical Data Analysis Software and Systems XXIII, ed. N. Manset & P. Forshay (San Francisco, CA: ASP), 391
Cutri, R. M., Wright, E. L., Conrow, T., et al. 2014, VizieR Online Data Catalog, II, 328
Douglas, D. H., & Peucker, T. K. 1973, Cartographica, 10, 112
Hennebelle, P., & Chabrier, G. 2008, ApJ, 684, 395
Hennemann, M., Motte, F., Schneider, N., et al. 2012, A&A, 543, L3
Hildebrand, R. H. 1983, QJRAS, 24, 267
Jones, E., Oliphant, T., Peterson, P., et al. 2001, SciPy: Open source scientific tools for Python, http://www.scipy.org/
Könyves, V., André, P., Men'shchikov, A., et al. 2015, A&A, 584, A91
Kraemer, K. E., Hora, J. L., Adams, J., et al. 2010, AAS Meeting, 215, 414.01
Kroupa, P. 2001, MNRAS, 322, 231
Kroupa, P., Weidner, C., Pflamm-Altenburg, J., et al. 2013, in The Stellar and Sub-Stellar Initial Mass Function of Simple and Composite Populations, ed. T. D. Oswalt & G. Gilmore, Vol. 5 (Berlin: Springer), 115
Lu, X., Cheng, Y., Ginsburg, A., et al. 2020, ApJL, 894, L14
Men'shchikov, A., André, P., Didelon, P., et al. 2012, A&A, 542, A81
Motte, F., & André, P. 2001, A&A, 365, 440
Motte, F., Andre, P., & Neri, R. 1998, A&A, 336, 150
Motte, F., Nony, T., Louvet, F., et al. 2018, NatAs, 2, 478
Offner, S. S. R., Clark, P. C., Hennebelle, P., et al. 2014, in Protostars and Planets VI, ed. H. Beuther et al. (Tucson, AZ: Univ. Arizona Press), 53
Roman-Duval, J., Jackson, J. M., Heyer, M., Rathborne, J., & Simon, R. 2010, ApJ, 723, 492
Rygl, K. L. J., Brunthaler, A., Sanna, A., et al. 2012, A&A, 539, A79
Salpeter, E. E. 1955, ApJ, 121, 161
Sanhueza, P., Contreras, Y., Wu, B., et al. 2019, ApJ, 886, 102
Sault, R. J., Teuben, P. J., & Wright, M. C. H. 1995, in ASP Conf. Ser. 77, Astronomical Data Analysis Software and Systems IV, ed. R. A. Shaw, H. E. Payne, & J. J. E. Hayes (San Francisco, CA: ASP), 433
Shadmehri, M., & Elmegreen, B. G. 2011, MNRAS, 410, 788
Solomon, P. M., Rivolo, A. R., Barrett, J., & Yahil, A. 1987, ApJ, 319, 730
Testi, L., & Sargent, A. I. 1998, ApJL, 508, L91
Tigé, J., Motte, F., Russeil, D., et al. 2017, A&A, 602, A77
Uyanıker, B., Fürst, E., Reich, W., Aschenbach, B., & Wielebinski, R. 2001, A&A, 371, 675
Wendker, H. J., Higgs, L. A., & Landecker, T. L. 1991, A&A, 241, 551
Williams, J. P., de Geus, E. J., & Blitz, L. 1994, ApJ, 428, 693
Williams, J. P., & McKee, C. F. 1997, ApJ, 476, 166